PERGAMON

International Journal of Plasticity 18 (2002) 1133–1163

INTERNATIONAL JOURNAL OF Plasticity

www.elsevier.com/locate/ijplas

A multiscale model of plasticity

Hussein M. Zbib[a,*], Tomas Diaz de la Rubia[b]

[a] *School of Mechanical and Materials Engineering, Washington State University, Pullman, WA 99164-2920, USA*

[b] *Materials Science and Technology Division, Chemistry and Materials Science Directorate, Mail Stop L-353, Lawrence Livermore National Laboratory, 7000 East Avenue, Livermore, CA 94550, USA*

Received in final revised form 20 July 2001

Abstract

A framework for investigating size-dependent small-scale plasticity phenomena and related material instabilities at various length scales ranging from the nano-microscale to the meso-scale is presented. The model is based on fundamental physical laws that govern dislocation motion and their interaction with various defects and interfaces. Particularly, the multi-scale framework merges two scales, the nano-microscale where plasticity is determined by explicit three-dimensional dislocation dynamics analysis providing the material length-scale, and the continuum scale where energy transport is based on basic continuum mechanics laws. The result is a hybrid elasto-viscoplastic simulation model coupling discrete dislocation dynamics with finite element analyses. With this hybrid approach, one can address complex size-dependent problems including, dislocation boundaries, dislocations in heterogeneous structures, dislocation interaction with interfaces and associated shape changes and lattice rotations, as well as deformation in nano-structured materials, localized deformation and shear bands.

Keywords: A. Dislocations, dynamics; B. Elastic-viscoplastic materials

1. Introduction

Plastic deformation in metals is a very complex phenomenon originating from highly nonlinear dynamical processes associated with microscopic defects, such as dislocations, voids, and microcracks. While dislocations and their mutual interactions determine the material strength in the absence of other internal defects, they tend to self-organize in the form of patterns, resulting into a heterogeneous field of

* Corresponding author. Tel.: +1-509-335-7832; fax: +1-509-335-4662.
E-mail address: zbib@mme.wsu.edu (H.M. Zbib).

0749-6419/02/$ - see front matter
PII: S0749-6419(01)00044-4

deformation at the microscale although the overall macroscopic field is thought to be homogeneous. Although there has been a tremendous effort to understand work hardening/strain softening and associated material instability phenomena, this research area is still in a parlous state, and rife with controversy. To some extent, this is due to the difficulty of carrying out truly definitive experiments on critical aspects of the evolution of the dislocation structure. But more important have been the immense theoretical difficulties of dealing with large numbers of dislocations and defects. Nonetheless, it is well understood that plastic deformation and strengthening in metals can be related to a number of heterogeneous patterns, such as dislocation cells, slip bands, microshear bands, persistent slip bands and dislocation tangles, which are critical for material properties (Essmann, 1964; Essmann and Mughrabi, 1979; Kuhlmann-Wilsdorf, 1998). For example, localized deformation, shear banding and dislocation cell structures play a significant role in determining the flow properties of heterogeneous materials, such as MMC, even at small macroscopic strains (Kamat and Hirth, 1990; Rhee et al., 1994). Dislocation pile-ups at the particle–matrix interface contribute to increased strength and changes in the interfacial properties, and the critical bowing out of a large number of dislocations could also explain shear banding leading to interfacial damage and debonding. Adiabatic shear banding has also been viewed as a leading mechanism in the formation of microcracks (Zbib and Jubran, 1992; Lambros and Rosakis, 1995).

The main difficulty in modeling the aforementioned phenomena lies in the fact that the length scale of these phenomena is not large enough to treat them within the realm of classical continuum mechanics framework. At the same time the length scale is not small enough to view these phenomena within the mechanics of a few dislocations, but rather through a thorough analysis of dislocation dynamics. For example, Kuhlmann-Wilsdorf (1998) proposed that the dislocation structures can be understood as a progression of low energy thermodynamic states with something like a conventional phase transition taking place between carpet structures and 3D cell structures at the end of Stage II (Kubin, 1993). In this same spirit, Holt (1970) proposed that dislocation structure evolution was akin to spinodal decompostion. Although his model was unphysical in important ways, his introduction of local densities of diffusing dislocation populations was adopted in later models. In particular, Aifantis (1987, 1988, 1995) and Walgraef and Schiller (1987) developed a model of dislocation patterning for slip bands and persistent slip bands. In this theory, third order reaction terms are essential for the development of ordering, and recent work of Kratochvil et al. (1997) has suggested that these terms arise when a mobile dislocation interacts with a dislocation dipole. But these reaction-diffusion schemes are quite simple, and do not yet address realistic 3D dislocation configurations.

The phenomena mentioned above, among others, illustrate the fact that deformation patterns, deformation induced hardening and structurally induced hardening are complex phenomena involving nonlinear interaction among dislocations and interaction of dislocations with interfaces. This further illuminates the fact that not the same deformation and strengthening mechanisms can explain these and many other phenomena. The length scale at which the deformation is taking place, the mode of deformation and structure size are important factors that determine the

corresponding dislocation mechanism. In this paper we present a framework for addressing small-scale plasticity phenomena based on discrete dislocation dynamics and continuum mechanics. In this framework, the plastic response of the material is determined by explicit evaluation of the evolution of dislocation population. The resulting hybrid model allows for rigorous investigation of deformation at the micro scale. In Section 2 we outline the general continuum mechanics framework for elasto-viscoplastic behavior with thermal effects. In Section 3, we present the discrete dislocation dynamics model and outline new techniques we developed recently to advance a previous model by Zbib and co-workers. In Section 4, the multiscale model is developed coupling the DD with continuum finite element analysis. Finally, in Section 5 a set of examples are presented in this paper including, deformation and lattice rotation induced by fundamental dislocation wall structures (pure tilt and pure twist walls), simulation of micro-shear bands, simulation of dislocation structure during the nanoindentation test, effect of boundary conditions on predicted stress–strain curves.

2. Elasto-viscoplastic continuum framework

Within the continuum mechanics framework, the governing equations of the material response are developed based on a *representative volume element (RVE)* over which the deformation field is assumed to be homogeneous. In this approach, the effect of internal defects, such as dislocations, voids, microcracks, etc., on material behavior and the manner they influence material properties is modeled through a set of internal variables and corresponding phenomenological evolution equations. Generally, the material response is measured in terms the macroscopic strain rate tensor $\dot{\boldsymbol{\varepsilon}}$ and its relation to the stress tensor $\mathbf{S}$. We consider a computational cell of size in the order of a few tens of micrometers containing many dislocations and point defects (microcracks, stacking fault tetrahedra, Frank sessile loops, rigid particles, etc.) as illustrated in Fig. 1 (Diaz de la Rubia et al., 2000). On the macroscale level, it is assumed that the material obeys the basic laws of continuum mechanics, i.e. the linear momentum balance:

$$\mathbf{div}\ \mathbf{S} = \rho\ \dot{\mathbf{v}} \tag{1}$$

and the energy equation

$$\boldsymbol{\rho}\ c_v \dot{T} = k\nabla^2 T + \mathbf{S}.\dot{\boldsymbol{\varepsilon}}^{\mathbf{p}} \tag{2}$$

where $\mathbf{v} = \dot{\mathbf{u}}$ is the particle velocity, $\mathbf{u}$, ρ, c_v and k are the displacement vector field, mass density, specific heat and thermal conductivity respectively. For elasto-viscoplastic behavior, the strain rate tensor $\dot{\boldsymbol{\varepsilon}}$ is decomposed into an elastic part $\dot{\boldsymbol{\varepsilon}}^e$ and a plastic part $\dot{\boldsymbol{\varepsilon}}^p$ such that

$$\dot{\boldsymbol{\varepsilon}} = \dot{\boldsymbol{\varepsilon}}^e + \dot{\boldsymbol{\varepsilon}}^p, \quad \dot{\boldsymbol{\varepsilon}} = \frac{1}{2}\left[\nabla\mathbf{v} + \nabla\mathbf{v}^{\mathbf{T}}\right] \tag{3}$$

For most metals the elastic response is linear and can be expressed by the incremental form of Hooke's law for large deformation and material rotation such that

$$\overset{\circ}{\mathbf{S}} = [\mathbf{C}^{\mathbf{e}}]\dot{\boldsymbol{\varepsilon}}^{\mathbf{e}}, \quad \overset{\circ}{\mathbf{S}} = \dot{\mathbf{S}} - \boldsymbol{\omega}\ \mathbf{S} + \mathbf{S}\ \boldsymbol{\omega}, \quad \boldsymbol{\omega} = \mathbf{W} - \mathbf{W}^{\mathbf{p}} \tag{4}$$

where $\mathbf{C}^{\mathbf{e}}$ is a fourth order tensor, $\boldsymbol{\omega}$ is the spin of the substructure and is given as the difference between the material spin $\mathbf{W}$ and plastic spin $\mathbf{W}^{\mathbf{p}}$. Combining (2) with (3) leads to

$$\overset{\circ}{\mathbf{S}} = [\mathbf{C}^{\mathbf{e}}]\left[\dot{\boldsymbol{\varepsilon}} - \dot{\boldsymbol{\varepsilon}}^{p}\right] \tag{5}$$

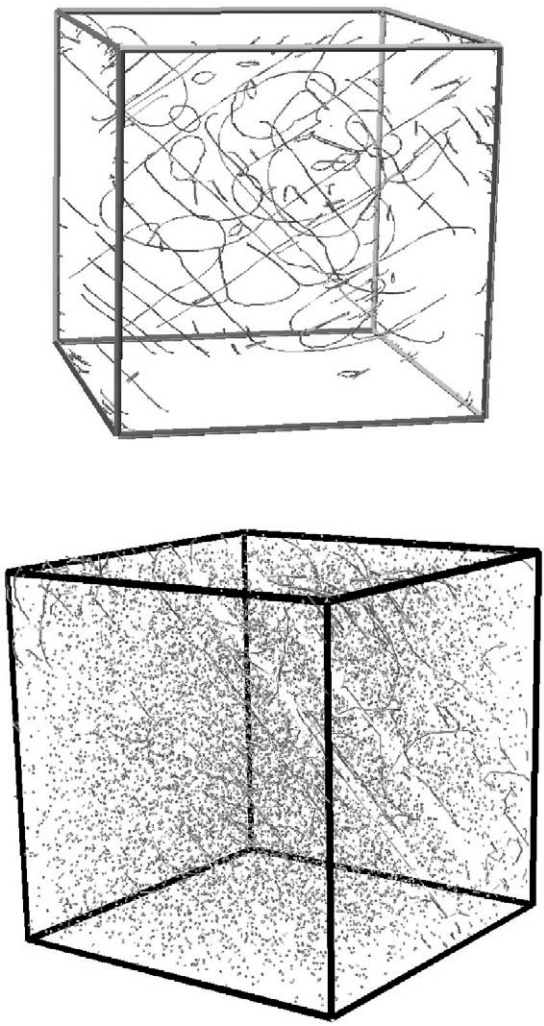

Fig. 1. Typical simulation cell containing (a) dislocations and (b) point defects.

The main challenge in the plasticity theory is the development of proper constitutive laws for $\dot{\varepsilon}^p$ and $\mathbf{W}^p$ (Voyadjis and Mohammad, 1991; McDowell, 1992; Khan and Chang, 1996; Le and Stumpf, 1996; Shizawa and Zbib, 1999; Houslby and Puzrin, 2000; Khan and Liang, 2000; Kalidindi, 2001; Scheidler and Wright, 2001). More importantly, these laws should be based on the underlying microstructure, mainly dislocations. Nonetheless, this task is perhaps formidable, especially when bridging two scales orders of magnitude apart, i.e. the continuum scale and the discrete dislocation scale. Here we emphasize that the *"assumed"* constitutive nature of $\dot{\varepsilon}^p$ and flow stress and their dependence upon internal variables and gradients of internal variables is very critical, since they dictate, among other things, the length scale of the problem and the phenomena that can be predicted by the model. In this respect, it goes without question that the most rigorous and physically based approach of computing the plastic strain and strain hardening in metals, with all relevant length scales, is through explicit evaluation of interaction, motion and evolution of all individual discrete dislocations and all relevant other defects in the crystal as described in the next section.

3. Description of the three-dimensional dislocation dynamics (DD)

The early discrete dislocation models were two-dimensional and consisted of periodic cells each with dislocations of Infinite length (Lepinoux and Kubin, 1987; Ghoniem and Amodeo, 1988; Groma and Pawley, 1993; Wang and LeSar, 1995). Later, a three-dimensional dislocation model was developed by Kubin et al. (1990) and Canova et al. (1993). In this model, dislocations are discretized into pure screw and edge segments of length restricted to be integer multiples of a minimum size. This scheme thus excludes mixed dislocations, requiring fine segmentation and producing an extremely large number of sub-segments during the simulations. These issues have been addressed in detail at by the recent work of Zbib et al. (1996, 1998), Hirth et al. (1996), and Rhee et al. (1998). In that work, arbitrarily curved dislocations are decomposed into piecewise continuous arrays of mixed straight segments and long-range interactions are treated using super-dislocations. The 3D discrete dislocation model *(micr3d)* developed at WSU simulates the dynamical behavior of large numbers of dislocations of arbitrary shapes, and interaction among groups of 3D dislocations. In the model, a crystal plasticity representation of a three dimensional crystal is considered containing a number of dislocation loops and lines of arbitrary shapes lying on primary and secondary slip systems as depicted in Fig. 1a and b. Dislocations in a fcc continuum are restricted to the $\{111\}<011>$ slip systems and, hence glissile dislocation lines can only lie on $\{111\}$ planes, with parallel planes being separated by the critical annihilation distance. For bcc single crystals the $\{110\}<111>$ and $\{112\}<111>$ are the most closed packed slip systems and both are active at low temperatures. The $\{123\}<111>$ slip systems are less closed packed and become active at high temperatures and will be included into the model at a later stage. The analysis is based on explicit evaluation of dislocation motion and their interaction with other defects and particles.

3.1. Computation of the dislocation stress field

The method developed by Zbib and co-workers for the computation of the dislocation stress field and dislocation-dislocation interaction is modified in this work to allow for fine resolution of segment length and to ensure numerical convergence as will be explained below.

Curved dislocations interact among themselves and with any applied stresses. In an exact treatment, the stress induced by an arbitrary dislocation loop at an arbitrary field point **P** (Fig. 2) can be computed by the Peach-Koehler equation given by the following line integral (Hirth and Lothe, 1982):

$$\begin{aligned}\sigma_{\alpha\beta}(\mathbf{p}) = &-\frac{G}{8\pi}\oint_C b_m \in_{im\alpha} \frac{\partial}{\partial x'_i}\nabla'^2 R \ \mathrm{d}x'_\beta - \frac{G}{8\pi}\oint_C b_m \\ &\in_{im\beta} \frac{\partial}{\partial x'_i}\nabla'^2 R \ \mathrm{d}x'_\alpha - \frac{G}{4\pi(1-\nu)}\oint_C b_m \\ &\in_{imk} \left(\frac{\partial^3 R}{\partial x'_i \partial x'_\alpha \partial x'_\beta} - \delta_{\alpha\beta}\frac{\partial}{\partial x'_i}\nabla'^2 R\right) \mathrm{d}x'_k \end{aligned} \tag{6}$$

where b_i is the (ith component of the) Burgers vector, $\in$ is the permutation symbol, G is the shear modulus, and ν is Poisson's ratio. The rest of the symbols are defined

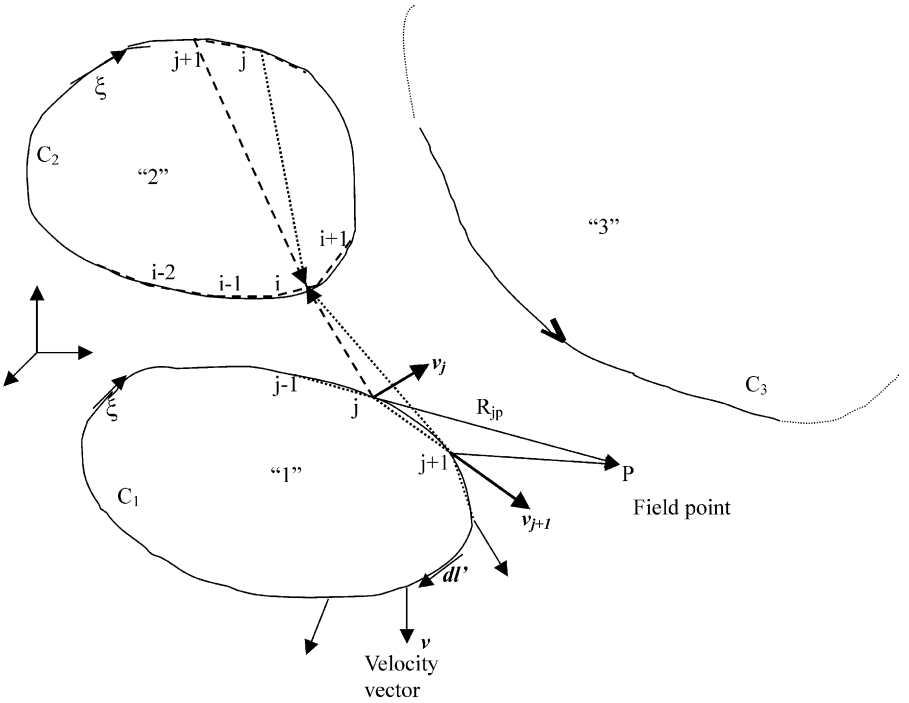

Fig. 2. Meshing: nodes and collocation points on dislocation loops and curves.

in Fig. 2. This integral can be evaluated numerically in a number of various methods. One method is to mesh the curve into set of nodal points as shown in the figure and perform piecewise integration so that

$$\sigma_{\alpha\beta}(\mathbf{p}) = \sum_{\text{allLoops}} \sum_{\mathbf{j}=1}^{n-1} \Bigg\{ -\frac{G}{8\pi} \int_{\mathbf{j}}^{\mathbf{j}+1} b_m \in_{im\alpha} \frac{\partial}{\partial x'_i} \nabla'^2 R \; \mathrm{d}x'_\beta - \frac{G}{8\pi} \int_{\mathbf{j}}^{\mathbf{j}+1} b_m \in_{im\beta} \frac{\partial}{\partial x'_i} \nabla'^2 R \; \mathrm{d}x'_\alpha - \frac{G}{4\pi(1-\nu)} \int_{\mathbf{j}}^{\mathbf{j}+1} b_m \in_{imk} \left(\frac{\partial^3 R}{\partial x'_i \partial x'_\alpha \partial x'_\beta} - \delta_{\alpha\beta} \frac{\partial}{\partial x'_i} \nabla'^2 R \right) \mathrm{d}x'_k \Bigg\} \tag{7}$$

where n is the total number of nodal points in a given loop or curve. Similar contributions arise from all loops as indicated by the first summation. The integral over the interval $\mathbf{j}$ to $\mathbf{j}+1$ can be evaluated explicitly using a straight segment approximation. The result is given in Hirth and Lothe (1982) and is indicated here as $\boldsymbol{\sigma}^{\mathbf{D}}_{\mathbf{j},\mathbf{j}+1} = \boldsymbol{\sigma}^{\mathbf{D}}_{\mathbf{j}+1} - \boldsymbol{\sigma}^{\mathbf{D}}_{\mathbf{j}}$. Then Eq. (7) reduces to the approximate form

$$\boldsymbol{\sigma}(\mathbf{p}) = \sum_{\mathbf{j}=1}^{N} \boldsymbol{\sigma}^{\mathbf{D}}_{\mathbf{j},\mathbf{j}+1} \tag{8}$$

where N is the total number of nodes from all loops and curves. This approximation can be very accurate even for a coarse mesh as can be deduced from Fig. 3. In the figure we compare the distributions of one of the stress components corresponding to a prismatic loop. The exact solution was obtained by solving Eq. (6) by Khraishi et al. (2000).

3.2. Self-force and Peach–Koehler (PK) force at dislocation nodes and segments

In order to compute the dynamics of the dislocation curve one needs to evaluate the local stress distribution and, therefore, the driving force and velocity distribution along the entire curve as depicted in Fig. 2. Numerically, this requires selecting a set of collocation points on the curve which are chosen to coincide with the dislocation nodes used to mesh the curve. So when the field point $\mathbf{p}$ is a collocation point, say point "i" in loop "2" as shown in Fig. 2, the stress at that point is determined from all other loops and loop "2" itself according to equation (8) except for the contribution from the portion bounded by the nodes $(i-1,i+1)$ of curve "2" where node "i" is located. For this portion a special treatment is required due to the singular character of the stress field when $R \to 0$ as can be deduced from Eq. (6). An approximate solution for this contribution in addition to the core energy has been developed by Zbib and co-workers by approximating the curve bounded by $i-1$ and $i+1$ as a simple dislocation bend, yielding a closed form analytical solution for the self-force $\mathbf{F}_{\mathbf{i}\text{-self}}$ at node "i". This approximation works well in terms of accuracy and

numerical convergence for segment length as small as $20b$. For finer segments, however, one can use a more accurate approximation by fitting the curve bounded by $i-1$ and $i+1$ to a simple circular arc the solution of which is given by Scattergood and Bacon (1975). Another treatment is given by Gavazza and Barnett (1976) and used in the recent work of Ghoniem and Sun (1999). Thus, using Eq. (8), the Peach–Kohler force computed directly on node "i" is given by

$$\mathbf{F_i} = \sum_{\mathbf{j}=1}^{N-1} \left(\boldsymbol{\sigma}^{\mathbf{D}}_{\mathbf{j},\mathbf{j}+1}(\mathbf{p}) + \boldsymbol{\sigma}^{\mathbf{a}}\mathbf{p} \right).\mathbf{b_i} \times \boldsymbol{\xi}_\mathbf{i} + \mathbf{F_{i-self}} \tag{9}$$

where $\boldsymbol{\sigma}^{\mathbf{a}}(p)$ is any other externally applied stress plus internal friction (if any) and stress induced by other defects such as stacking fault tetrahedra (SFT's) and Franks sessile loops (for irradiation hardening problems), interaction with rigid particles (for metal matrix composites problems), and interaction with internal and external

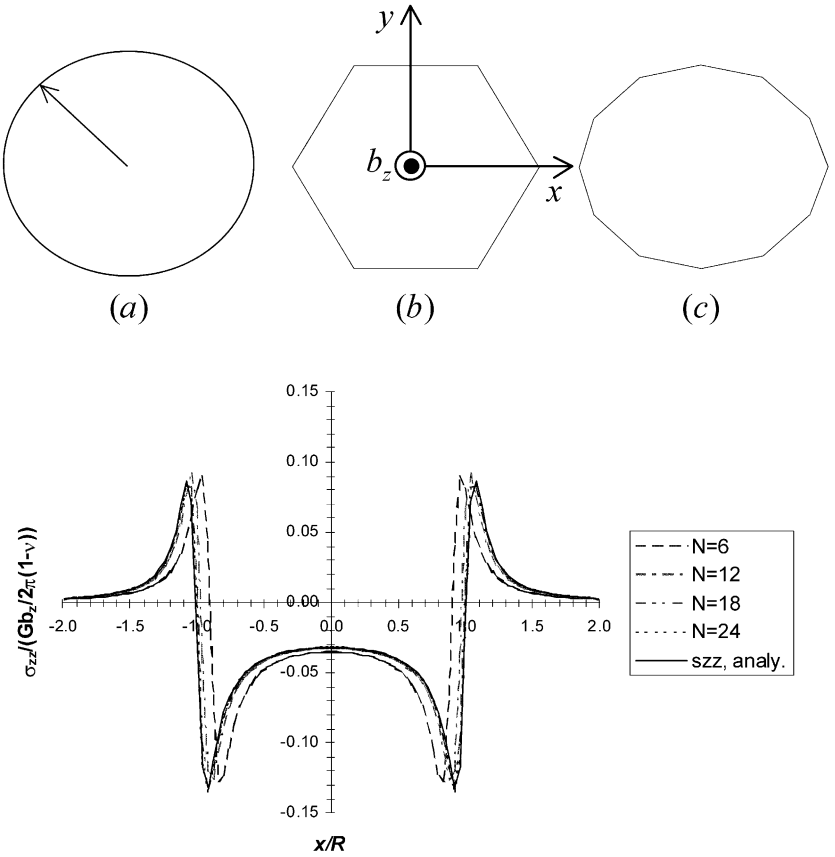

Fig. 3. The stress distribution of a prismatic loop. Comparison between the exact analytical solution (from Khraishi et al., 2000) and approximate solution for various segment size.

free surfaces (for micro-cracks problems). In Eq. (9), $\mathbf{b_i}$ is the Burgers vector, and $\boldsymbol{\xi}_\mathbf{i}$ is the line sense. With this treatment, the dislocation curves are approximated as continuous arrays of mixed segments as illustrated in Fig. 2 but when computing the local stress (self force) the curve is smoothed into a simple circular arc, permitting fine resolutions with accurate results and convergence as discussed in the next section.

The direct computation of the PK force at the nodes as discussed above requires the use of very fine mesh, especially when dealing with problems involving dislocation-defect interaction. As a general rule the dislocation segment size (distance between two adjacent nodes) must be comparable to the size of the defect or the nearby dislocation segment, otherwise the computation of the interaction may not be accurate. To remedy this problem, the PK force is integrated over the entire segment length. Namely, consider a dislocation segment bounded by nodes j and $j+1$, then the PK force on the segment is integrated over the entire segment length L such that

$$\mathbf{F_{j,j+1}} = \sum_{\mathbf{i}=1}^{N-1} \frac{1}{L} \int_{\mathbf{L}} \left(\boldsymbol{\sigma}^{\mathbf{D}}_{\mathbf{i,i+1}}(\mathbf{p}) + \boldsymbol{\sigma}^{\mathbf{a}}(\mathbf{p})\right).\mathbf{b_{j,j+1}} \times \boldsymbol{\xi}_{\mathbf{j,j+1}} dl + \mathbf{F_{j,j+1self}} \tag{10}$$

where $\mathbf{p}$ is a field point on the dislocation segment j, $j+1$ and $\mathbf{F}_{\text{self}}$ is that corresponding to the local interaction between the segment adjacent to $j,j+1$ and are treated in the same manner discussed above. Numerically, this leads to integration over a number of n gauss points and (10) becomes

$$\mathbf{F_{j,j+1}} = \sum_{\mathbf{i}=1}^{N-1} \frac{1}{n} \sum_{\mathbf{k}=1}^{\mathbf{n}} \boldsymbol{\sigma}^{\mathbf{D}}_{\mathbf{i,i+1}}(\mathbf{p_k}) + \boldsymbol{\sigma}^{\mathbf{a}}(\mathbf{p_k}).\mathbf{b_{j,j+1}} \times \boldsymbol{\xi}_{\mathbf{j,j+1}} + \mathbf{F_{j,j+1self}} \tag{11}$$

where $\mathbf{p_k}$ is the gauss point k. Once the segment PK is computed it is distributed equally to its nodes j and $j+1$. This is analogous to the load distribution method used in the finite element analysis.

3.3. Equations of motion

In the dislocation dynamics, all N *dislocation nodes* ($3\times N$ degrees of freedom) move simultaneously in the glide direction over a characteristic time corresponding to the least time increment required for an interaction to take place, such as two dislocations to annihilate or form a junction. The result is a set of nonlinear differential equations governing the motion of the dislocation segments. The governing equation of glide motion for each dislocation node is given by (Hirth et al., 1998) which when combined with (11) leads to

$$m^*_\mathbf{i}\dot{\mathbf{v}}_\mathbf{i} + \frac{1}{M_\mathbf{i}(T,p)}\dot{\mathbf{v}}_\mathbf{i} = \mathbf{F}_{\mathbf{i}\text{glide-component}} \tag{12}$$

Here m^* *is* the effective mass per unit dislocation, M is the mobility which could depend on both temperature T and pressure p, and it could also be a fuction of the

angle between the Burgers vector and the dislocation line sense, especially at low temperatures. For example, in bcc single crystals, at low temperatures a pure screw dislocation has a rather complex three-dimensional core structure, resulting in a high Pierels stress which is overcome by stress-assisted thermal activation (Hirth and Lothe, 1982). This leads to a relatively low mobility for screw dislocations while the mobility of mixed dislocations is very high (Urabe and Weertman, 1975). For dislocations moving at high speeds Hirth et al. (1998) derived the following expressions for the effective mass m^* per unit dislocation length

$$m_s^* = \frac{W_0}{v^2}\left(-\gamma^{-1} + \gamma^{-3}\right) \tag{13}$$

for screw dislocation and for the edge dislocation

$$m_e^* = \frac{W_0 C^2}{v^4}\left[-16\gamma_l - 40\gamma_l^{-1} + 8\gamma_l^{-3} + 14\gamma + 50\gamma^{-1} - 22\gamma^{-3} + 6\gamma^{-5}\right] \tag{14}$$

where $\gamma_l = \left(1 - v^2/C_l^2\right)^{1/2}$, $\gamma = \left(1 - v^2/C^2\right)^{1/2}$, C_l is the longitudinal sound velocity and C is the transverse sound velocity, and W_0 is the rest energy for the screw. In treatments of acceleration, an impulse load is assumed to be applied to the dislocation so that the core accelerates to a new velocity after a brief relaxation time (b/C) where b is the length of the Burgers vector. Through a period equal to the relaxation time to achieve a new steady state, the long-range strain field is moving at a different velocity than the core. Thus, an oscillatory, quasi-steady state is possible with the long-range strain field oscillating about the core position. However, Beltz et al. (1968) showed that the oscillations can be described in terms of Eq. (10), with the associated energy radiation contributing M. Similarly, the possibility of an instability consisting of the faceting of the line into a non-straight shape can be treated in terms of the Lagrangian L Hirth et al. (1998). For low velocities (less than one tenth the transverse sound velocity) the inertia term is very small and can be neglected.

The set of Eqs. (12) are coupled and highly nonlinear. They are solved simultaneously using an implicit scheme as described later which turns out to be stable provided that the integration time step is small enough, which is the case here as dictated by the short-range interaction. Then each dislocation node is advanced to a new position over an increment of time. In the new configuration, the spacing between any two adjacent nodes may become larger than a pre-assigned maximum allowable length (e.g. $5-50b$, depending on the nature and size of the problem) in which case a new node is assigned at mid-point of the two nodes.

In passing we point out that the above treatment is different than the one originally developed by Zbib et al. (1996; 1998) where the PK force and velocity vector were evaluated at the center of the segment "$j-j+1$" then the nodal values, say at node "j" were taken as the average of those corresponding to the adjacent segments. The current treatment makes better approximation of the local curvature for the self-force as well as integrating the PK force over the entire length of the curve, ensuring numerical accuracy and convergence.

3.4. Short-range reactions and cross-slip

Short-range interactions considered in the model include annihilation, and formation of dipoles, jogs and junctions. A short-range interaction occurs when the distance between two dislocations becomes comparable to the size of the core where the elasticity field is no longer valid. With the meshing described above, mixed dislocations of arbitrary characters can be easily introduced. Therefore, junctions are explicitly formed during the simulations. A complete list of the short-range interaction rules for dislocation dynamics is given by Rhee et al. (1998).

Cross-slip is an important mechanism in recovery processes in both fcc and bcc metals. Screw dislocations may cross-slip to reduce internal stresses and to circumvent internal obstacles, consequently, providing a mechanism for the production of Frank–Read sources through double cross-slip. This process is a thermally activated process and, therefore, is more prolific at high temperatures. Therefore, cross-slip is determined numerically using a Monte-Carlo type simulation where the probability of a segment to jump into a secondary plane is determined by the probability P, accounting for segment length and activation energy to cross-slip (Rhee et al., 1998), which is given by

$$P = \alpha \ \Omega_1 \ \delta \ t \exp\left(-\frac{\Delta W^* - \tau A}{kT}\right), \quad \Omega_1 = \frac{C_t \pi}{L} \tag{15}$$

where Ω_1 is the fundamental frequency of a vibrating dislocation segment of length L, C_t is the transverse sound velocity, δt is the time increment, α is a numerical parameter controlling the frequency of cross slip, $\Delta \mathbf{W}^*$ is the activation energy to form a kink configuration as discussed by Rhee et al. (1998) (not to be confused with the double kink activation energy) plus constriction energy, τ is the resolved shear stress, A is the area swept by the dislocation segment, k is the Boltzmann constant, T is the absolute temperature.

3.5. Dislocation-induced plastic distortion

The motion of each dislocation segment contributes to the overall macroscopic plastic strain $\dot{\boldsymbol{\varepsilon}}^{\mathbf{p}}$ and plastic spin $\mathbf{W}^{\mathbf{p}}$ via the relations:

$$\dot{\boldsymbol{\varepsilon}}^{p} = \sum_{i=1}^{N} \frac{l_i v_{gi}}{2V} (\mathbf{n_i} \otimes \mathbf{b_i} + \mathbf{b_i} \otimes \mathbf{n_i}), \tag{16}_1$$

$$\mathbf{W}^{\mathbf{p}} = \sum_{i=1}^{N} \frac{l_i v_{gi}}{2V} (\mathbf{n_i} \otimes \mathbf{b_i} - \mathbf{b_i} \otimes \mathbf{n_i}), \tag{16}_2$$

$$\dot{\mathbf{n}} = \boldsymbol{\omega} \mathbf{n} \tag{16}_3$$

where l_i is the segment length, $\mathbf{n_i}$ is a unit normal to the slip plane, v_{gi} is the magnitude of the glide velocity, and N is the total number of segments. In (16) "V" is the

volume of the RVE which is the finite element in the FEA for the finite domain problems. When the simulation cell is a representative cell in an infinite domain (and only DD analysis is performed) "V" is the volume of the entire cell. Furthermore, for the discrete dislocation system, one can also calculate the dislocation density tensor $\boldsymbol{\alpha}$

$$\boldsymbol{\alpha} = \sum \frac{l_i}{V} \mathbf{b_i} \otimes \boldsymbol{\xi}_\mathbf{i} \tag{17}$$

This quantity provides a direct measure for the net Burgers vector that gives rise to strain gradient relief (bending of crystal). The above system of equations provides the most rigorous connection between the dislocation motion (the fundamental mechanism of plastic deformation) and the macroscopic plastic strain, with its dependence on strength and applied stress being explicitly embedded in the calculation of the velocity of each dislocation. Moreover, nonlocal effects are explicitly included into the calculation through long-range interactions.

4. The multi-scale boundary value problem

For *infinite domain* problems, the computational cell as a whole is considered as a representative volume element. In the dislocation dynamics analysis we employ either reflection boundary conditions as described by Zbib et al. (1998) which ensures continuity of dislocation curves, or periodic boundary conditions as given recently by Bulatov et al. (2000) which ensures conservation of dislocation flux across boundaries as well as continuity. However, for *finite domain* problems and those involving internal surfaces and heterogeneous media, these methods are no longer valid and a more rigorous treatment of boundary conditions is required. This issue is treated below.

4.1. The superposition principle—homogenous materials

4.1.1. Interaction with external free surfaces

The solution for the stress field of a dislocation segment [Eq. (6)] is known for the case of infinite domain and homogeneous materials, which is used in DD codes. Therefore, the principle of superposition [also used by Van der Giessen and Needleman (1995) and Needleman (2000) for the 2D case, and was extended to 3D by Fivel et al. (1998) and Yasin et al. (2001)] is employed to correct for the actual boundary conditions, for both finite domain and homogenous materials. The method assumes two solutions as depicted in Fig. 3. Assuming that dislocation segments, dislocations loops and any other internal defects with self induced stress (e.g. cracks can be modeled as pile-ups of dislocation Demir and Zbib, in press) are situated in a finite domain V bounded by ∂V and subjected to arbitrary external

traction and constraints as shown in Fig. 4. Then the stress field is given by the sum of two solutions:

$$\begin{aligned} \mathbf{S} &= \mathbf{S}^{\infty} + \mathbf{S}^{*} \\ \mathbf{u} &= \mathbf{u}^{\infty} + \mathbf{u}^{*} \\ \boldsymbol{\varepsilon} &= \boldsymbol{\varepsilon}^{\infty} + \boldsymbol{\varepsilon}^{*} \end{aligned} \tag{18}$$

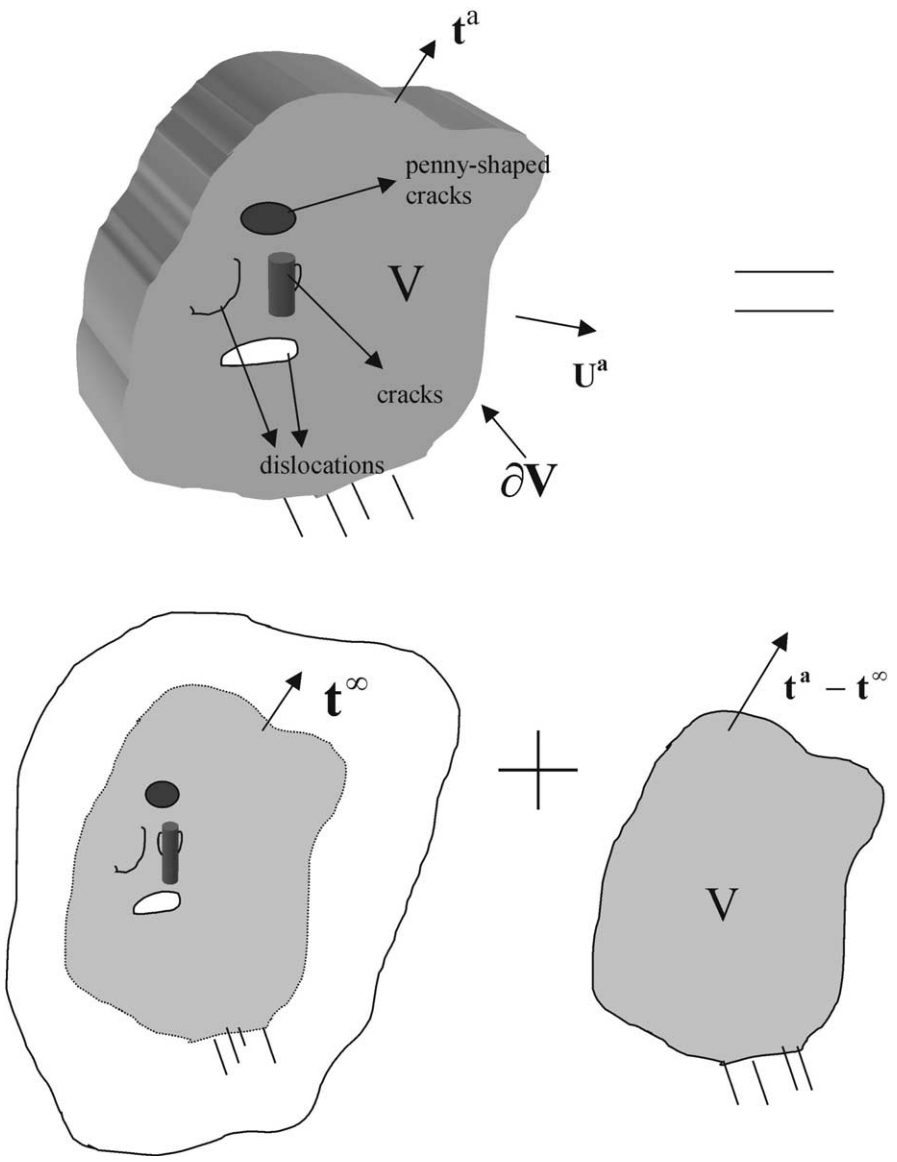

Fig. 4. Coupled *DD–FEA* boundary value problem using the superposition principle.

where $\mathbf{S}^{\infty}$, $\boldsymbol{\varepsilon}^{\infty}$ and $\mathbf{u}^{\infty}$ are the stress field, strain field and displacement fields, respectively, caused by the internal defects as if they were in an infinite domain, whereas $\mathbf{S}^{*}$, $\boldsymbol{\varepsilon}^{*}$ and $\mathbf{u}^{*}$ are the fields corresponding to the auxiliary problem satisfying the following boundary conditions

$$\begin{aligned} &\mathbf{t} = \mathbf{t}^{\mathbf{a}} - \mathbf{t}^{\infty} \quad \text{on } \partial\mathbf{V} \\ &\mathbf{u} = \mathbf{u}^{\mathbf{a}} \quad \text{on part of } \partial\mathbf{V} \end{aligned} \tag{19}$$

where $\mathbf{t}^{\mathbf{a}}$ is the externally applied traction, and $\mathbf{t}^{\infty}$ is the traction induced on ∂V by the defects (dislocations) in the infinite domain problem. The traction $-\mathbf{t}^{\infty}$ on ∂V results into an *image stress* which is superimposed onto the dislocations segments and, thus, accounting for surface-dislocation interaction.

4.1.2. Internal surfaces

The treatment discussed above considers interaction between dislocations and external surfaces, as well as internal free surfaces such as voids. Internal surfaces such as micro-cracks and rigid surfaces around fibers, say, are treated within the dislocation theory framework, whereby each surface is modeled as a pile- up of infinitesimal dislocation loops. Hence defects of these types are all represented as dislocation segments and loops, and their interaction with external free surfaces follows the method discussed above. This subject is discussed in a separate article (Kharishi et al., 2001).

4.1.3. Dislocation stress as an internal variable

The *long-range stress* field arising from the dislocations is computationally expensive (N^2 problem, N is the number of dislocation segments). A numerical technique method termed the *superdislocation method* and based on the multipolar expansion (Wang and LeSar, 1995) method has been outlined by Zbib et al. (1998) which reduces the order of the problem to $N\log N$ with high accuracy. In this method dislocations far away from the point of interest are grouped together into a set of equivalent monopoles and dipoles. Here we present another approach more consistent with the finite element framework which captures both the dislocation-self stress and its distortion. Consider a *RVE*, then the stress field induced by the dislocations contained within the *RVE* can be treated as an internal stress $\mathbf{S}^{\mathrm{D}}$ (homogenized over the finite element with enough gauss points) as illustrated in Fig. 5. Moreover, the effective total stress within the *RVE* is the sum of the stress by all external agencies $\mathbf{S}$ and the internal stress $\mathbf{S}^{\mathrm{D}}$. Hence, the constitutive equation in total form becomes:

$$\mathbf{S} + \mathbf{S}^{\mathbf{D}} = [\mathbf{C}^{\mathbf{e}}]\,[\boldsymbol{\varepsilon} - \boldsymbol{\varepsilon}^{\mathbf{p}}], \quad \mathbf{S}^{\mathbf{D}} = <\boldsymbol{\sigma}^{\mathbf{D}}> = \frac{1}{V_{\text{element}}}\int_{\text{element}} \boldsymbol{\sigma}^{\mathbf{D}}(x)\mathrm{d}\mathbf{v} \tag{20}$$

Since the dislocation stress field varies as $1/r$, careful approximation of $\mathbf{S}^{\mathbf{D}}$ over the *RVE* is important.

4.1.4. The finite element formulation—solid mechanics

Without loss of generality, Eqs. (3) and (5) can be re-written in total form as in (17) (as opposed to the rate form) and the system of equations can be cast into a standard finite element framework (the formulation for the rate-form follows along the same lines but involves additional terms and will be left for future treatment) which has the following general form.

$$[\mathbf{M}]\left\{\ddot{\mathbf{U}}\right\} + [\mathbf{C}]\left\{\dot{\mathbf{U}}\right\} + [\mathbf{K}]\{\mathbf{U}\} = \{\mathbf{f^a}\} + \left\{\mathbf{f^B}\right\} + \{\mathbf{f^\infty}\} + \left\{\mathbf{f^P}\right\} \tag{21}$$

where $[M] = \int_V \rho[N]^{\mathbf{T}}[N]\mathrm{d}v$ is the mass matrix, $[\mathbf{K}] = \int_V [\mathbf{B}]^{\mathbf{T}}[\mathbf{C^e}][\mathbf{B}]\mathrm{d}v$ is the stiffness matrix, $\{\mathbf{f^a}\} = \int_{\mathbf{s}} \mathbf{t^a}[\mathbf{N}]\mathrm{d}s$ is the applied force vector, $\{\mathbf{f^\infty}\} = \int_{\mathbf{s}} \mathbf{t^\infty}[\mathbf{N}]\mathrm{d}s$ is the force vector from dislocation image stresses, $\left\{\mathbf{f^B}\right\} = \int_{\mathbf{v}} \mathbf{S^D}[\mathbf{B}]\mathrm{d}\mathbf{v}$ is the body force vector from dislocations long-range interaction and $\left\{\mathbf{f^P}\right\} = \int_{\mathbf{v}} [\mathbf{C^e}]\boldsymbol{\varepsilon}^{\mathbf{P}}[\mathbf{B}]\mathrm{d}\mathbf{v}$ is force vector from plastic strain caused by dislocations, with [**N**] being the shape function vector, [**B**] = grad[**N**], {u} = [N]{U}, $\boldsymbol{\varepsilon} = [B]\{U\}$, and [**C**] is the damping matrix. Dislocations are sorted out in each element and they contribute to the plastic strain based on Eq. (16).

The numerical treatment of the dislocation long-range stress described above, using the internal stress concept ($\mathbf{S^D}$), results into the body-force vector $\{\mathbf{f^B}\}$. Thus, the resulting stress field in each element includes stress from all external agencies and dislocations. And therefore, the driving force on each dislocation is readily evaluated from this stress field. This approximation works well for far apart dislocation-dislocation interaction (dislocations not residing in the same element). The interaction of dislocations belonging to the same element must be computed one-to-one (M^2, M = number of dislocation segments in a given element). For example, consider dislocation segment j–j + 1 in an element containing M dislocations, then Eq. (11) is replaced by

$$\mathbf{F_{j,j+1}} = \sum_{\mathbf{i}=1}^{\mathbf{M}-1} \frac{1}{n} \sum_{\mathbf{k}=1}^{\mathbf{n}} \boldsymbol{\sigma}^{\mathbf{D}}_{\mathbf{i},\mathbf{i}+1}(\mathbf{p_k}) + \boldsymbol{\sigma}^{\mathbf{a}}(\mathbf{p_k}) + \mathbf{S} - \mathbf{S^D}.\mathbf{b_{j,j+1}} \times \boldsymbol{\xi}_{\mathbf{j,j+1}} + \mathbf{F_{j,j+1self}} \tag{22}$$

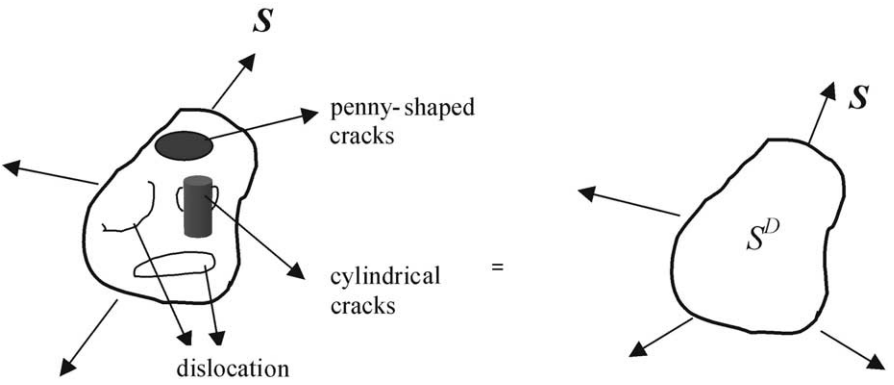

Fig. 5. Representative volume element: (a) inhomogeneous containing defects, (b) homogenous with an equivalent internal stress (eigenstress).

with $\mathbf{S}$ being the total stress in the element computed from the *FEA* described above and $\mathbf{S^D}$ is the homogeneous internal stress from dislocations within the element.

4.1.5. The finite element formulation—heat transfer

The energy Eq. (2) is also solved using the finite element method leading to the standard form:

$$[\mathbf{C_T}]\left\{\dot{\mathbf{T}}\right\} + [\mathbf{K_T}]\{\mathbf{T}\} = \{\mathbf{f_T}\} \tag{23}$$

where $[\mathbf{C_T}] = \int_V \boldsymbol{\rho}\mathbf{c}[N]^{\mathbf{T}}[N]\mathrm{d}v$ is the damping matrix arising from the term on the right-hand side of equation (2), $[\mathbf{K_T}] = \int_V \mathbf{k}[\mathbf{B}]^{\mathbf{T}}[\mathbf{B}]\mathrm{d}v$ is the stiffness matrix arising from the heat conduction term and $\{\mathbf{f_T}\} = \int \mathbf{S}.\dot{\boldsymbol{\varepsilon}}^{\mathbf{p}}[\mathbf{N}]\mathrm{d}\mathbf{v}$ is the load vector arising from the plastic energy term.

4.1.6. Numerical solution—explicit integration

The multiscale model described above is implemented into a numerical code with variety of options depending on the loading conditions. Full dynamic analysis (*DD* and *FEA*) or *DD* with quasi-static *FEA* [by simply dropping the first two terms in (21)] can be performed.

The dislocation equation of motion (12) is solved using an *implicit* algorithm by evaluating the equation at time $t+\delta t$ along with a backward integration scheme, yielding the recurrence equation

$$\mathbf{v_i^{t+\delta t}}\left(1+\frac{\Delta t}{m^* M}\right)_{\mathbf{i}}^{\mathbf{i+\delta t}} = \mathbf{v_i^t} + \frac{\Delta t}{m^*}\mathbf{F_i^{t+\delta t}} \tag{24}$$

It can be shown that this integration scheme is unconditionally stable for any time step size. However, the *DD* time step is dictated by both the shortest flight distance for short-range interactions, as well as the dynamic finite element model which is solved using a forward explicit integration scheme. This scheme is chosen since the time step in the *DD* analysis (for high strain rates) is of the same order of magnitude of the time required for stable explicit *FE* dynamic analysis (*FEA*). In this analysis, the critical time t_c and the time step for both the *DD* and the *FEA*, which yield a stable solution, are given by $\mathbf{t_c} = \frac{l_c}{C_l}$, $\boldsymbol{\delta t} = \frac{\mathbf{t_c}}{\mathbf{20}}$ where $l_{\mathbf{c}}$ is the characteristic length scale which is the shortest dimension in the finite element mesh.

4.1.7. Extension to inhomogeneous materials

The model described above for dislocations in homogenous materials has been implemented into a finite element code. The model can be extended to the case of dislocations in heterogeneous materials using the concept of superposition as follows.

4.1.7.1. Case 1: dislocations in one sub-domain. Suppose that domain V is divided into two sub-domain V_1 and V_2 with domain V_1 containing a set of dislocations. The stress field induced by the dislocations and any externally applied stresses in both domains can be constructed in terms of two solutions, *i*.

$$\begin{aligned} \mathbf{S} &= \mathbf{S}^{\infty 1} + \mathbf{S}^{*}, \\ \boldsymbol{\varepsilon} &= \boldsymbol{\varepsilon}^{\infty 1} + \boldsymbol{\varepsilon}^{*} \end{aligned} \tag{25}$$

where $\mathbf{S}^{\infty 1}$ and $\boldsymbol{\varepsilon}^{\infty 1}$ are the stress field and strain field, respectively, caused by the dislocations (the infinite solution) with the entire domain V having the same material properties of domain V_1 *(homogenous solution)*. Applying Hooke's law for each of the sub-domains, and using (21), we obtain the elastic constitutive equations for each of the materials in each of the sub-domains as:

$$\begin{aligned} &\mathbf{S}^{*} = \left[\mathbf{C}_1^{\mathbf{e}}\right]\boldsymbol{\varepsilon}^{*}, && \text{in} \quad V_1 \\ &\mathbf{S}^{*} = \left[\mathbf{C}_2^{\mathbf{e}}\right]\boldsymbol{\varepsilon}^{*} + \boldsymbol{\sigma}^{*21}; \quad \boldsymbol{\sigma}^{*21} = \left[\mathbf{C}_2^{\mathbf{e}} - \mathbf{C}_1^{\mathbf{e}}\right]\boldsymbol{\varepsilon}^{\infty 1}, && \text{in} \quad V_2 \end{aligned} \tag{26}$$

where $\mathbf{C}_1^{\mathbf{e}}$ and $\mathbf{C}_2^{\mathbf{e}}$ are the elastic stiffness tensors in V_1 and V_2, respectively. The boundary conditions are:

$$\begin{aligned} &\mathbf{t} = \mathbf{t}^{\mathbf{a}} - \mathbf{t}_1^{\infty} && \text{on } \partial V \\ &\mathbf{u} = \mathbf{u}^{\mathbf{a}} && \text{on part of } \partial V \end{aligned} \tag{27}$$

where $\mathbf{t}^{\mathbf{a}}$ is the externally applied traction and $\mathbf{t}_1^{\infty}$ is the traction induced on all of ∂V by the dislocations in V_1 in the infinite-homogenous domain problem. The "*eigenstress*" $\boldsymbol{\sigma}^{\infty 21}$ is due to the difference in material properties.

4.1.7.2. Case 2: dislocations in two sub-domains. Suppose that both sub-domains contain dislocations (and/or other defect with self inducing stress fields). The method of superposition described above can be extended by dividing the solution into three parts such that

$$\begin{aligned} \mathbf{S} &= \mathbf{S}^{\infty 1} + \mathbf{S}^{\infty 2} + \mathbf{S}^{*}, \\ \boldsymbol{\varepsilon} &= \boldsymbol{\varepsilon}^{\infty 1} + \boldsymbol{\varepsilon}^{\infty 2} + \boldsymbol{\varepsilon}^{*} \end{aligned} \tag{28}$$

where $\mathbf{S}^{\infty 1}$ and $\boldsymbol{\varepsilon}^{\infty 1}$ are the stress and strain fields (infinite solution) from dislocations in domain V_1 with V being homogenous with properties of V_1, and $\mathbf{S}^{\infty 2}$ and $\boldsymbol{\varepsilon}^{\infty 2}$ are the stress and strain fields (infinite solution) from dislocations in domain V_2 with V being homogenous with properties of V_2. This leads to the elastic constitutive equations

$$\begin{aligned} &\mathbf{S}^{*} = \left[\mathbf{C}_1^{\mathbf{e}}\right]\boldsymbol{\varepsilon}^{*} + \boldsymbol{\sigma}^{*12}; \quad \boldsymbol{\sigma}^{*12} = \left[\mathbf{C}_1^{\mathbf{e}} - \mathbf{C}_2^{\mathbf{e}}\right]\boldsymbol{\varepsilon}^{\infty 2} && \text{in} \quad V_1 \\ &\mathbf{S}^{*} = \left[\mathbf{C}_2^{\mathbf{e}}\right]\boldsymbol{\varepsilon}^{*} + \boldsymbol{\sigma}^{*21}; \quad \boldsymbol{\sigma}^{*21} = \left[\mathbf{C}_2^{\mathbf{e}} - \mathbf{C}_1^{\mathbf{e}}\right]\boldsymbol{\varepsilon}^{\infty 1}, && \text{in} \quad V_2 \end{aligned} \tag{29}$$

4.1.7.3. Case 3: generalization to N sub-domains. The method described above can be easily extended to the case of heterogeneous materials with N sub-domains leading to the following relations.

$$\begin{aligned} \mathbf{S} &= \sum_{\mathbf{i}=1}^{\mathbf{N}} \mathbf{S}^{\infty \mathbf{i}} + \mathbf{S}^{*}, \\ \boldsymbol{\varepsilon} &= \sum_{\mathbf{i}=1}^{\mathbf{N}} \boldsymbol{\varepsilon}^{\infty \mathbf{i}} + \boldsymbol{\varepsilon}^{*} \end{aligned} \tag{30}$$

with the constitutive equation

$$\mathbf{S}^* = \left[\mathbf{C}_\mathbf{i}^\mathbf{e}\right](\boldsymbol{\varepsilon}^* - \boldsymbol{\varepsilon}^\mathbf{p}) + \sum_{\mathbf{j}=1}^{\mathbf{N}} \boldsymbol{\sigma}^{*\mathbf{ij}}; \quad \boldsymbol{\sigma}^{*\mathbf{ij}} = \left[\mathbf{C}_\mathbf{i}^\mathbf{e} - \mathbf{C}_\mathbf{j}^\mathbf{e}\right]\boldsymbol{\varepsilon}^{\infty\mathbf{j}} \quad \text{in} \quad V_i$$
$$i = 1, 2, \ldots N \tag{31}$$

The *eigenstress* $\boldsymbol{\sigma}^{*\mathbf{ij}}$, in turn, contributes to the body-force vector $\{f^B\}$ in Eq. (18). The method is similar to that developed by Van der Giessen and Needleman (1995) for the 2D case.

The three models described above, i.e. the *DD* model (*micro3d*), the solid mechanics (*fea3d*) and the heat transfer (*ht3d*), are coupled into a unified system as summarized in Fig. 6 yielding a hybrid *multiscale model* of plasticity (*msm3d*) which has the following features:

1. couples the continuum dynamics problem (elastic-plastic waves) with the dislocation dynamics problem,
2. deals directly with all possible boundary, interfaces and dislocations in heterogeneous materials,
3. incorporates shape changes associated with dislocation motion and distortions,
4. incorporates directly dislocation long-ranges stresses, and
5. incorporates lattice distortion (elastic) that arises from dislocations.

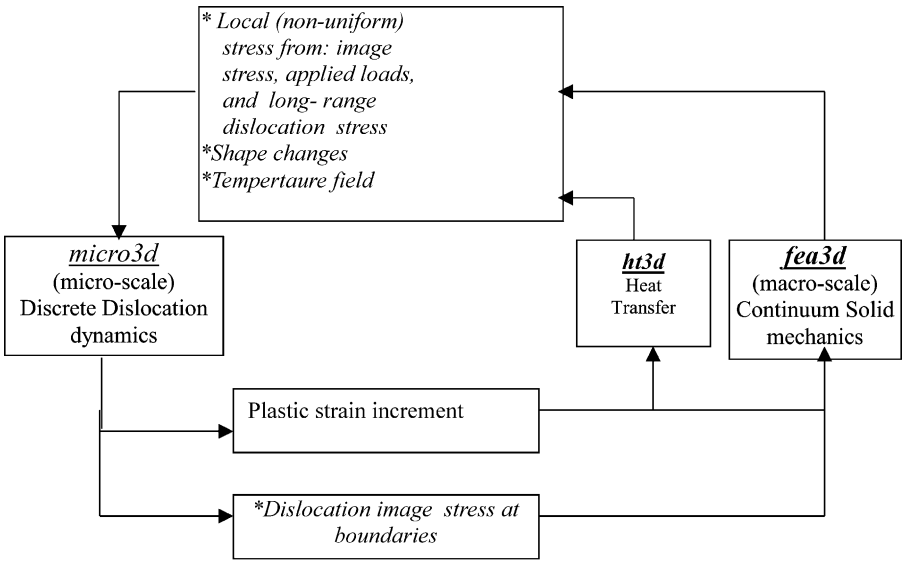

Fig. 6. Summary of the multiscale model of plasticity.

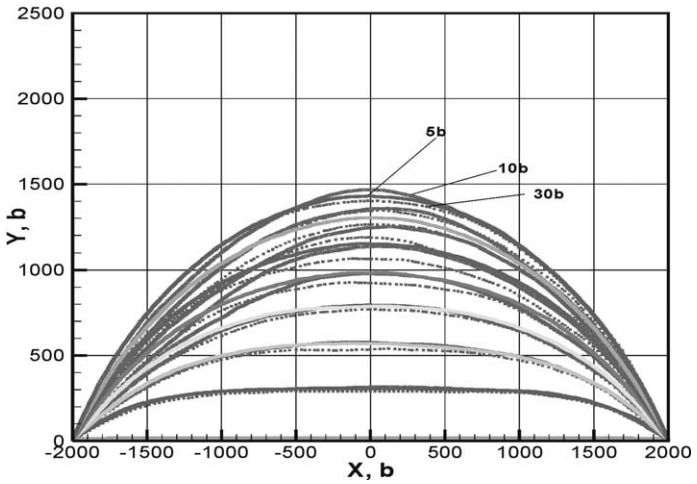

Fig. 7. Effect of dislocation mesh size (segment length). Pure edge dislocation, under an applied shear stress of 13 MPa.

5. Application to various plasticity phenomena

In the simulations discussed below eight-node brick elements with eight integration points are used. The space is nondimensionalized by the magnitude of the Burgers vector (b). The purpose of the simulations presented below is to illustrate the capability of the msm3d model in capturing various plasticity phenomena at nano-microscale as well as the mesoscale. It is emphasized that the full multiscale dynamic model has already been implemented into a numerical code. Below we present analyses for static loading conditions only where the inertia and damping terms in Eq. (21) are dropped. Results for dynamic and thermal analyses for high strain phenomena will be presented in other articles.

5.1. Dislocation mesh refinement and convergence

First we examine the effect of the dislocation mesh size on the numerical results. As discussed above, the dislocation curve is meshed into a set of nodes, forming the degrees of freedom, and segments. The smaller the spacing between two adjacent nodes, or smaller segment length, the more degrees of freedom are introduced into the simulations, increasing the computational effort. The mesh size, therefore, should depend on the nature and size of the problem that one is investigating. Nevertheless, the analysis should converge towards a stable configuration as the mesh is refined. This is illustrated in this example where we consider a simple Frank–Read (FR) source shown in Fig. 7. The material consider is a copper single crystal with the following properties (relevant to both the continuum model and the *DD* model) $\mu = 54.6$ MPa, $\nu = 0.324$, $\rho_m = 8900$ kg/m^3, $b = 2.56\text{x } 10^{-10}$ m, and $M = 1000.0$ Pa^{-1}.s^{-1} (dislocation mobility). The source is subjected to a constant shear stress of

13 MPa. The time step used in the numerical integration is maintained constant at 10^{-12} s. The integration was performed for various mesh sizes (segment length and nodal spacing) ranging from 5*b* to 30*b*. The result for the cases of 5*b*, 10*b* and 30*b* is shown in Fig. 7. The plots correspond to the position of the bow-out dislocation for every 50 integration steps. It can be seen from the figure that the three mesh sizes produces almost the same configurations. The CPU time for the case of 5b was almost four times larger than that of the 30*b* case.

5.2. Dislocation self-stress and surface distortion

Next we show that the *msm3d* model is capable of capturing geometric distortions and stress fields induced by the dislocations. Figs. 8 and 9 show the results for cases of pure edge and pure screw dislocations respectively. In both cases the dislocation is initially situated at the center of the specimen whose size is $400\times400\times800$ *b*, with FE element size of $40\times40\times80$ *b* ($10\times10\times25$ nm). The bottom of the specimen is held constant while the upper surface is subjected to a constant shear stress. The stress contours shown in the figures are those induced by the dislocation. Also shown is the macroscopic plastic strain produced by the dislocation motion. The geometric distortion associated with this motion is also shown in the figure (the displacement is magnified by a factor of 20), clearly showing the development of a "smoothed ledge" at the surface, albeit its size is dictated by the *FE* mesh size. The displacement and stress fields obtained by the *msm3d* model are as expected for the pure and edge dislocations.

5.3. Dislocation-surface interaction: micro-bands

Next we consider a specimen with a single Frank-Read source subjected to a constant axial stress of 100 MPa as shown in Fig. 10. The specimen ($10{,}000\times10{,}000\times20{,}000$ *b*) is held constant at the bottom surface and loaded in the *z*-direction. All other surfaces are free. Dislocations emit from the FR source (corresponding to the slip system $(1\bar{1}1)[10\bar{1}]$) as depicted in Fig. 10b and annihilate at the surfaces. Continuous emission of dislocations results into an increase in the local plastic strain rate. Fig. 11 shows the results for the case of double-slip when two FR sources are activated as can be deduced from the figure, corresponding to the slip systems $(1\bar{1}1)[10\bar{1}]$and $(\bar{1}\bar{1}1)[011]$, forming microshear bands and resulting into surface distortions.

5.4. Dislocation boundaries: bending and torsion of lattice structure

The *msm3d* model can be used to analyze complex dislocation boundaries and structures to shed some lights on what controls hardening in metals at small scale. This is rather important to understand when trying to model the material behavior using macroscopic concepts such as those used in strain gradient theories. One of those concepts is related to the so-called geometrically necessary boundaries (Hughes et al., 2001). Two fundamental walls are examined, the pure tilt wall which

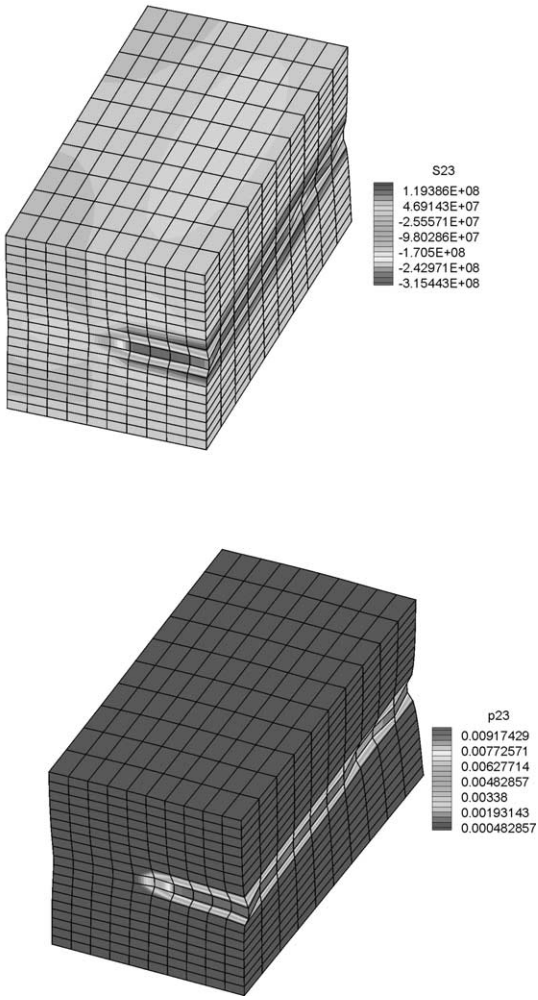

Fig. 8. Stress, plastic strain and distortion induced by a pure edge dislocation as predicted by the msm3d model. Element size 40*b*.

is made up of pure edge dislocations and the pure twist wall which consists of two sets of pure screw dislocation normal to each other (Hirth and Lothe, 1982) as can be seen in Fig. 12. For both cases the dislocation spacing is 500 *b*, corresponding to an angle of rotation of 0.12 degrees for the case of an infinite wall. However, here the walls are finite and the external surfaces are free, thus the rotation they induce is larger than that of the infinite wall. The presence of the dislocation walls causes the crystal to bend in the case of the tilt wall and twist in the case of the twist boundary as can be deduced from Fig. 12. In both cases the boundaries are assumed to be free with the specimen fixed at the left x–y plane. It is pointed out that in the case of free boundaries it is very important to account for image stresses as indicated by the

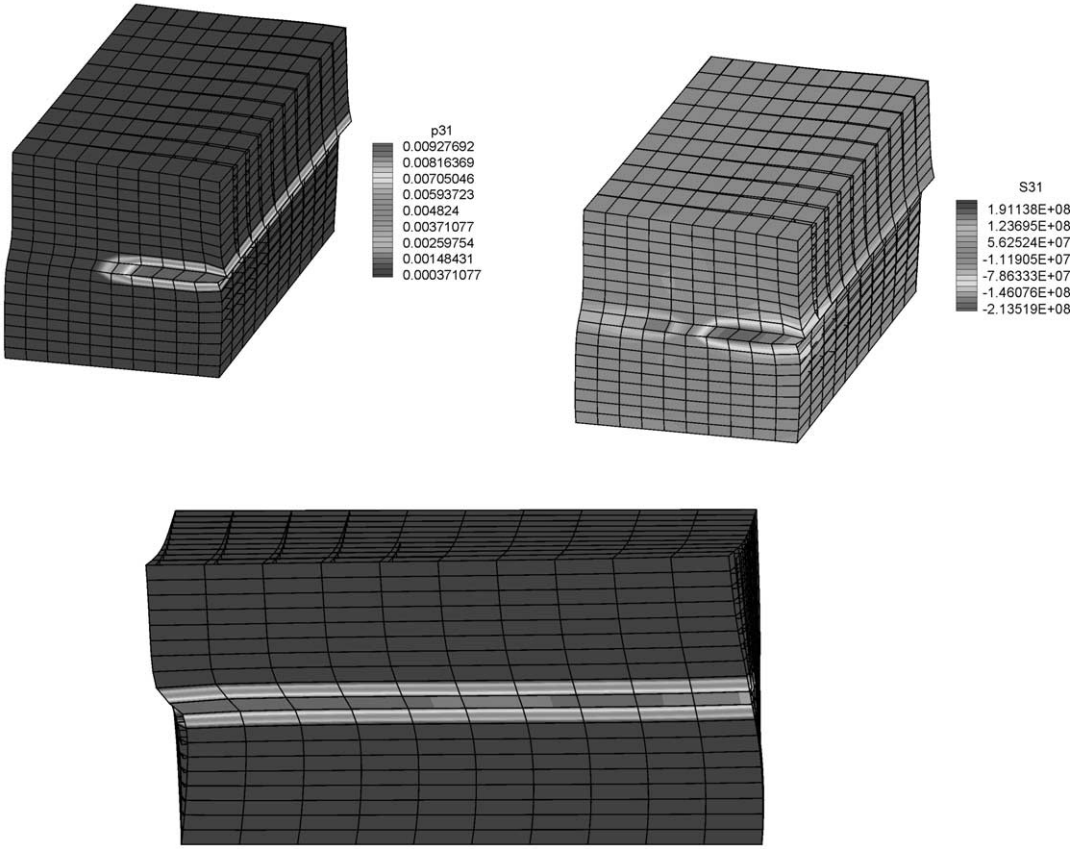

Fig. 9. Stress, plastic strain and distortion induced by a pure screw dislocation as predicted by the msm3d model. Element size 40*b*. Displacement is magnified by a factor of 20.

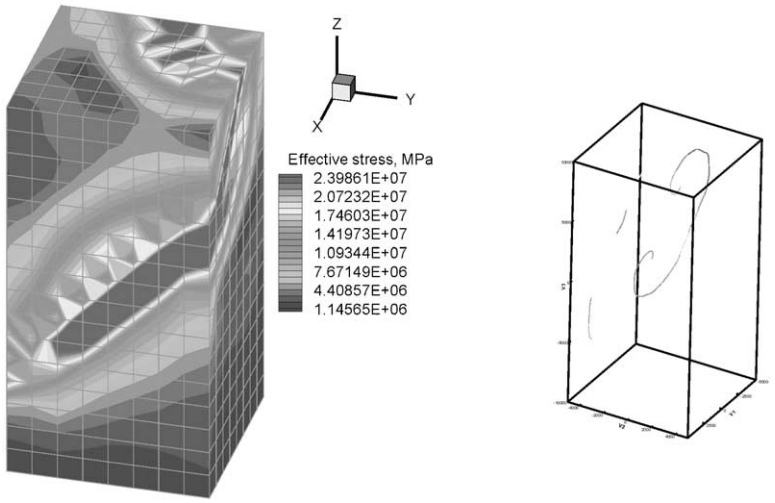

Fig. 10. Simulation of dislocation emission from a Frank–Read source with free boundary condition subjected to a constant axial stress of 100 MPa.

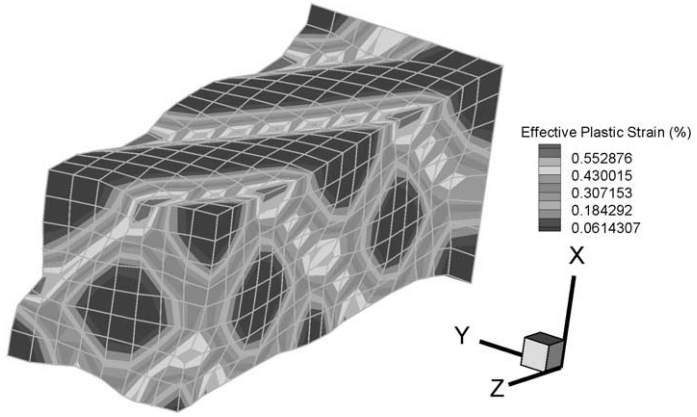

Fig. 11. Distribution of effective plastic strain rate for the case of double slip under constant stress with free boundary condition, showing the development of steps at the surfaces. (Deformed configuration with displacement magnified by a factor of 100.)

term **f** in Eq. (21). If this is not account for the result one gets is very much different in terms of distortion as well as the stress fields. For finite walls the stress field has a long range character as discussed by Hughes et al. (2001).

5.5. *Effect of free surfaces and cell size on predicted yield stress*

The effect of image stresses and the significance of dislocation-boundary interaction on prediction of macroscopic properties is illustrated in this simulation. Here we consider the case of a rectangular parallelepiped sample containing dislocation

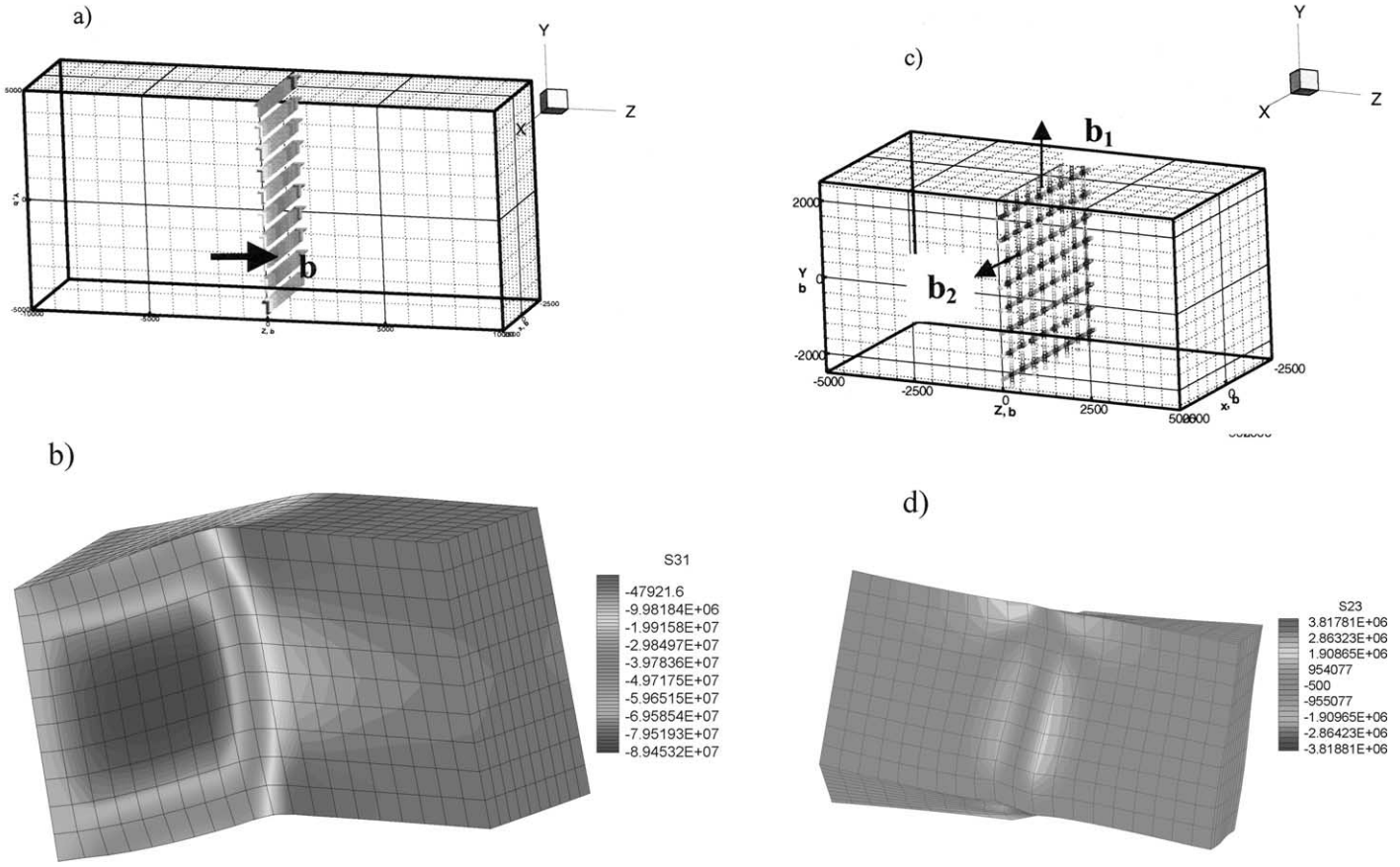

Fig. 12. Lattice distortion caused by dislocation as predicted by the msm3d model. (a) Pure tilt wall of edge dislocations resulting into (b) bending (tilt boundary), and (c) twist boundary of two families of pure screw dislocations resulting into pure twist (d). (Displacement is magnified by a factor of 20.)

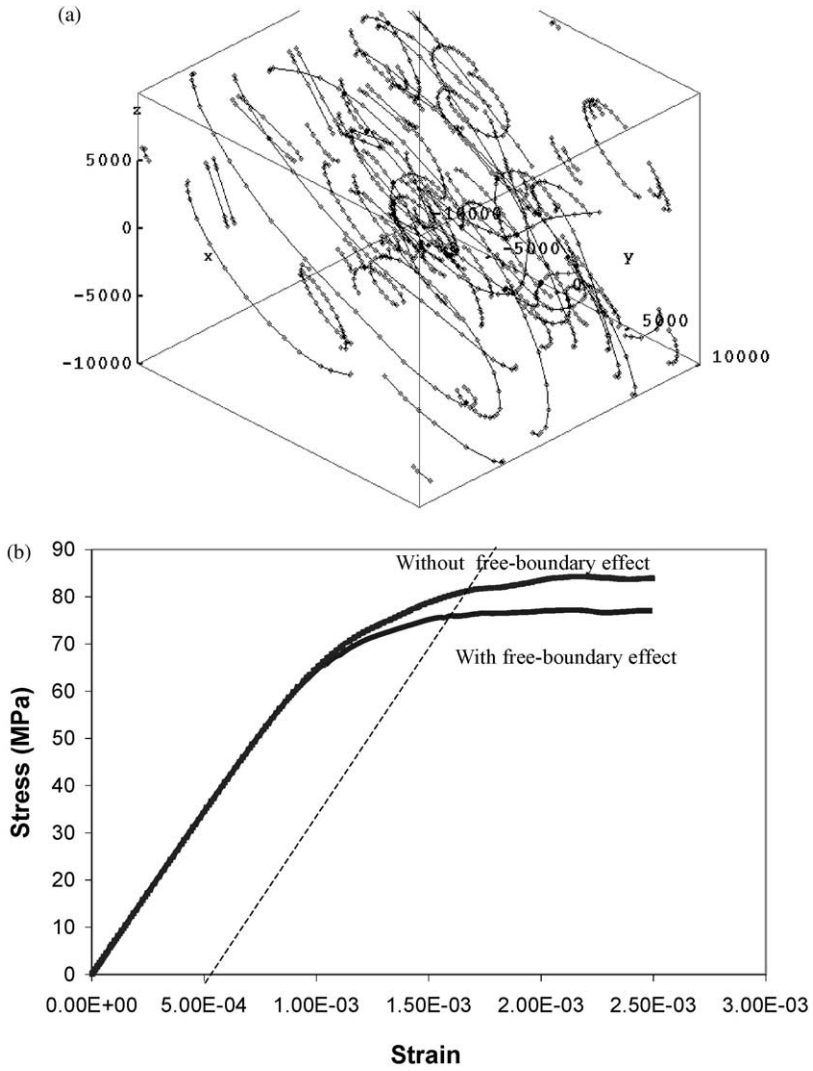

Fig. 13. Crystal size = 20,000*b* (5.72 μm). (a) Dislocation sources start operating, as the resolved shear stress is greater than the critical shear stress. Dislocation density increases with strain as more dislocation segments are generated. All sources generate dislocations in the (111) plane (single slip). (b) Effect of the free boundaries on the stress-strain curve for cubic Aluminum single crystal. The 0.05% yield is 75.9 MPa when the free surface effect is applied, while it is 81.4 MPa when it is neglected.

lines and/or loops and examine the effect of free surfaces on dislocation behavior. The sample shown in Fig. 13a is divided into $10\times10\times10$ eight-node elements. Tractions at free surfaces, resulting from dislocations, are computed at four integration points. The bottom surface of the sample is fixed, and the upper surface is moved at controlled rate so that the average strain rate is maintained constant ($1/s$) (the displacement of the upper surface is incremented in time). All other surfaces are

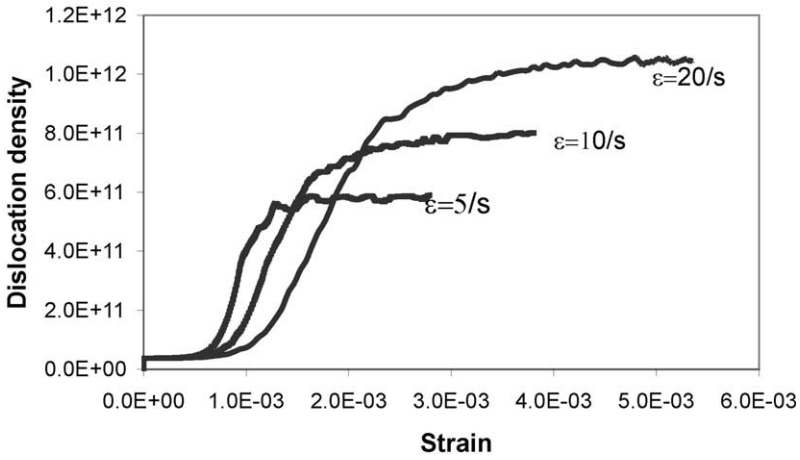

Fig. 14. Evolution of dislocation density with strain for different strain rates.

assumed to be free. The analysis is performed for an aluminum single crystal whose properties are: $\mu = 26.6$ MPa, $\nu = 0.334$, $\rho_m = 2800$ kg/m^3, $b = 2.862e^{-10}$ m, and $M = 1000.0$ Pa^{-1}.s^{-1}.

Forty Frank–Read sources were distributed randomly with random length ranging from 4000b (1.144 μm) to 6000b (1.716 μm) in a cubic aluminum single crystal (Fig. 13a) with side dimension of 20,000b (5.72 μm). The analysis was performed for a wide range of cell size (20,000 to 50,000b) and strain rates, only a representative sample is given here. All the dislocation sources were located on the (111) planes for a random distribution of three different Burgers directions of $[1\bar{1}0]$, $[10\bar{1}]$ and $[0\bar{1}1]$. The crystal was loaded uniaxially under constant strain rate of 10 s^{-1} in the [0 0 1] direction. The intent of this example is to show the effect of boundary condition on the resulting stress-strain curve. Hence, and for numerical reasons only, we consider low dislocation density as can be deduced from Fig. 14.

Fig. 13a shows a typical dislocation configuration. The dislocation sources start operating when the resolved shear stress on the dislocation reaches the critical shear stress. The resulting stress-strain curves are shown in Fig. 13b. The figure shows the difference between the strength of the crystal when the free-boundary effect (image stress) is applied and when it is neglected. The percentage difference is about 7% calculated at 0.05% yield strength. Of course this difference in behavior can be attributed to image stresses. For the crystal with the free boundary, the dislocation density stays constant until the dislocation sources start operating (Fig. 14). The magnitude of the flow stress is mainly dictated by the size of the FR source (i.e. the distance between the two pinned ends of the source) and the size of the simulation cell, or simply the average size of the dislocation mean free path. In principle, stress required to propagate a dislocation form a FR source is inversely proportional to the source size (values more consistent with experiments require the simulation of larger simulation cells with higher dislocation density and periodic boundary conditions; a task which is being undertaken and the results will be reported in a future

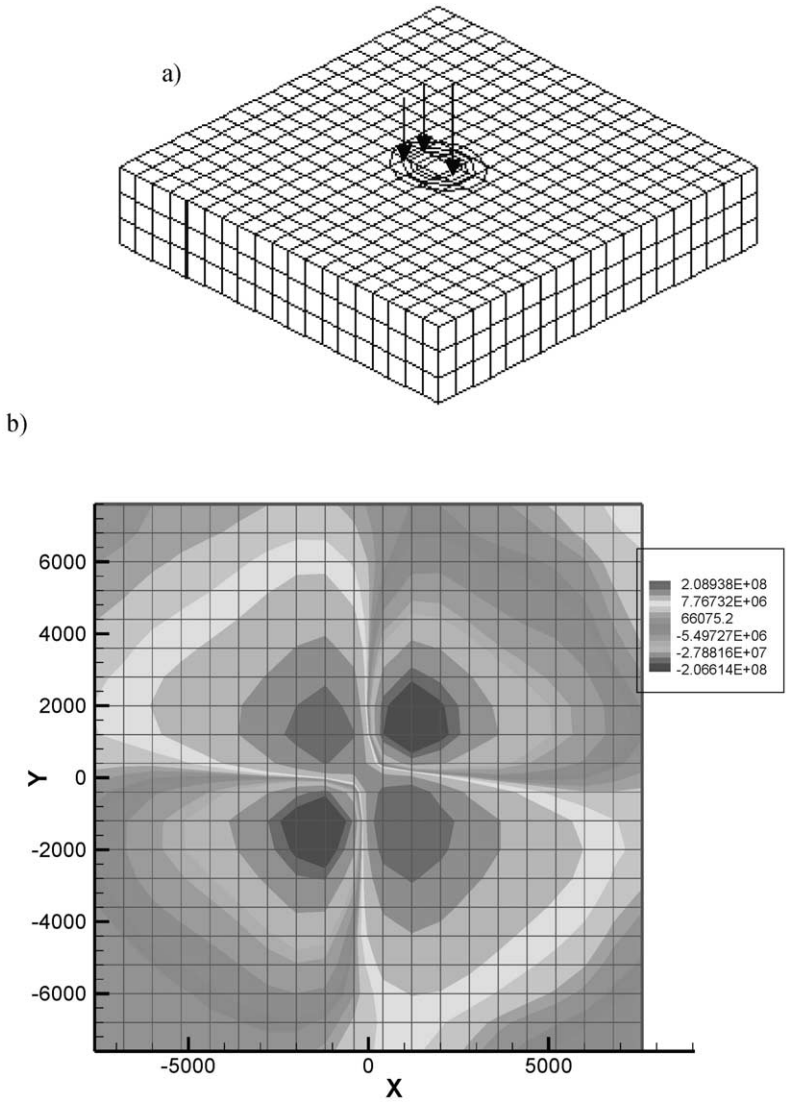

Fig. 15. The nanoindentation simulation, the *FEA* mesh and stress contour.

article). When the sources start operating, the dislocation density increases up to a saturation value at which the portion of the dislocation segments generated by the sources are equalized by the dislocation segments disappearing on the free surface and by dislocation-dislocation annihilation. As the strain rate increases, the saturation value of the dislocation density increases as can be deduced from Fig. 14. The effect of the cell size on the results was also investigated for the same dislocation source distribution. The size of the crystal was increased to 22,000b (6.29 μm), 30,000b (8.58 μm) and 40,000b (11.44 μm. The result showed that one ***should not***

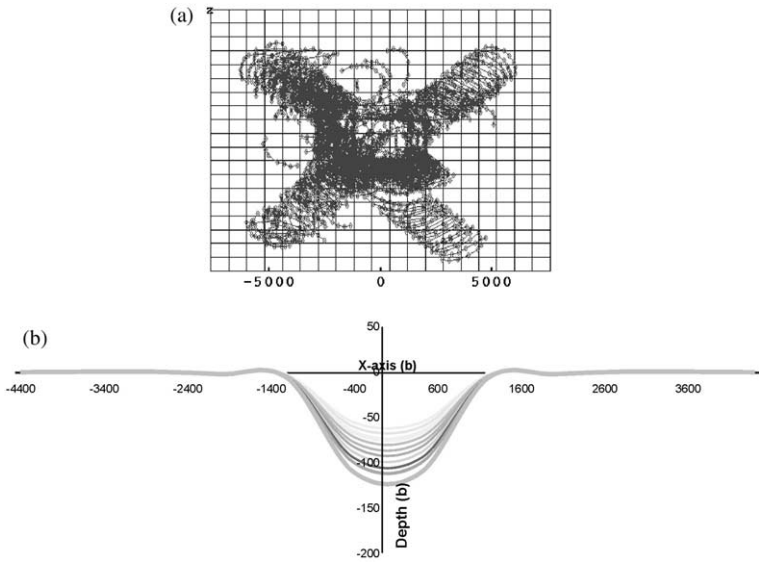

Fig. 16. Results of the nanoindentation simulations. (a) Developed dislocation structure underneath the indenter, and (b) the predicted indentation depth showing the development of surface distortions.

simply neglect the effect of the boundaries on the stress–strain curve regardless of the size of the cell. Similar results are given in the work of Yasin et al. (2001).

5.6. Nanoindentation

With the *msm3d* model one can also investigates deformation and strength in thin-layered structures. Here we present results pertaining to the nanoindentation test. A variety of shapes and sizes of indenters can be used for different goals. In this study, the focus is on spherical indenters with nano-meter size scale. The indenter has 192 nm radius of curvature ("Berkovich" style indenter), and the test sample is Fe–3% Si single crystal with $\mu = 81.4$ MPa, $\nu = 0.29$, $\rho_{m=}7870$ kg/m^3, $b = 2.4\text{x}10^{-10}$ m, side dimension = 3–4 mm Oxide thin film, thickness = 10.0 nm, $\mu = 120$ MPa, $\nu = 0.25$.

An experiment was performed to compare the results with the *msm3d* results and were reported in Bahr and Zbib (submitted). First, the sample was loaded, then a hold segment was applied for creep to take place and then the sample is unloaded to a certain point after which a hold was applied to measure instrument drift, and finally the sample was unloaded. The load was applied normal to the (001) plane. For the numerical simulations using the *msm3d* model, the sample is a rectangular parallelepiped with 3.65 μm (15,200 *b*) in width, 3.65 μm (15,200 *b*) in depth and 0.72 μm (3000 *b*) in thickness (Fig. 15a). This size is considered sufficiently large to deal with 192 nm-indenter radius. The simulated sample was divided into $19\times19\times3$ elements. The size of each element is $192\times192\times240$ nm. The dimensions of the element are selected to be of the same size as the indenter diameter for the sake of simplicity in applying the load. The load is applied on the element(s) in the middle of the upper

(001) surface in such away that the load is distributed on one element when it is less that 50% of the maximum load. Thereafter it is distributed on nine elements such that 20% of the load is applied on the middle element surface and the rest of the load is equally distributed on the other eight elements surfaces. Selecting one or nine elements surfaces gives the closest approximation to the circular area of contact during indentation and distributing the load this way is a good approximation to the Hertz pressure distribution expected during contact. The base of the sample is fixed in all directions. Several initial dislocation distribution configurations are used: one dislocation source, two dislocation sources and random distribution close to the area of contact, the length of the sources ranges between 1000 and 1200b. The stress field during nanoindentation is shown in Fig. 15b. For the case of random distribution of dislocation sources, the evolution of dislocations is shown in Fig. 16a and the depth during nanoindentation as predicted by *msm3d* is shown in Fig. 16b. The resulting dislocation structure and predicted depth are consisted with experimental observations reported by Zielinski et al. (1995) and Bahr and Zbib (submitted).

In conclusion, a multiscale model coupling 3D discrete dislocation dynamics with continuum finite element model based on elasto-viscoplasticity has been developed. A method based on the super-position principle is outlined for modeling dislocation-surface interactions in both homogeneous and heterogeneous materials. It is suggested that this new hybrid approach provides an explicit means for investigating complex small-scale plasticity phenomena, including surface effects, ledges, micro-schear bands, dislocation boundaries, deformation of thin layers.

Acknowledgements

The support of Lawrence Livermore National Laboratory to WSU is gratefully acknowledged. This work was performed, in part, under the auspices of the U.S. Department of Energy by Lawrence Livermore National Laboratory (contract W-7405-Eng-48). We like to thank Robb Thomson for fruitful discussions about some aspects of the short-range reactions and the cross-slip model.

References

Aifantis, E.C., 1987. The physics of plastic deformation. Int. J. Plasticity 3, 211–247.

Aifantis, E.C., 1988. On the problem of dislocation patterning and persistent bands. Sol. Stat. Phenom. 3&4, 397–406.

Aifantis, E.C., 1995. Pattern formation in plasticity. Int. J. Eng. Sci. 33, 2161–2178.

Bahr, D., Zbib, H.M., 2001. Didslocation dynamics modeling of nanoindentation experiments (submitted).

Beltz, R.J., Davis, T.L., Malén, K., 1968. Phys. Stat. Solid 26, 621.

Bulatov, V.V., Rhee, M., Cai, W., 2000. Periodic boundary conditions for dislocation dynamics simulations in three dimensions. Proceedings of the MRS meeting.

Canova, G., Brechet, Y., Kubin, L.P., Devincre, B., Pontikis, V., Condat, M., 1993. 3D simulation of dislocation motion on a lattice: application to the yield surface of single crystals. In: Rabiet, J. (Ed.), Microstructures and Physical Properties. CH-Transtech.

Demir, I. and Zbib, H.M., in press. A mesoscopic model for inelastic deformation and damage. Int. J. Eng. Science.

Diaz de la Rubia, T., Zbib, H.M., Victoria, M., Wright, A., Khraishi, T., Caturla, M., 2000. Flow localization in irradiated materials: a multiscale modeling approach. Nature 406, 871–874.

Essmann, U., 1964. Elektronenmikroskopische Untersuchung der Versetzungsanordnung. Plastisch Verformten Kupfereinkristallen, Acta Metall. 12, 1468–1470.

Essmann, U., Mughrabi, H., 1979. Annihilation of dislocations during tensile and cyclic deformation of limits of dislocation densities. Phil. Mag. A 40 (6), 731–756.

Fivel, M.C., Roberston, C.F., Canova, G., Bonlanger, L., 1998. Three-dimensional modeling of indent-induced plastic zone at a mesocale. Acta Mater. 46 (17), 6183–6194.

Gavazza, S.D., Barnett, D.M., 1976. The self-force on a planar dislocation loop in an anisotropic linear-elastic medium. J. Mech. Phys. Solids 24, 171–185.

Ghoniem, N.M., Amodeo, R.J., 1988. Computer simulation of dislocation pattern formation. Sol. Stat. Phenome. 3 & 4, 379–406.

Ghoniem, N.M., Sun, L., 1999. A fast sum method for the elastic field of 3-D dislocation ensembles. Phys. Rev. B. 128–140.

Groma, I., Pawley, G.S., 1993. Role of the secondary slip system in a computer simulation model of the plastic behavior of single crystals. Mater. Sci. Eng. A164, 306–311.

Hirth, J.P., Lothe, J., 1982. Theory of Dislocations. Wiley, New York.

Hirth, J.P., Rhee, M., Zbib, H.M., 1996. Modeling of deformation by a 3D simulation of multipole, curved dislocations. J. Computer-Aided Materials Design 3, 164–166.

Hirth, J.P., Zbib, H.M., Lothe, J., 1998. Forces on high velocity dislocations. Modeling & Simulations in Maters. Sci. & Enger. 6, 165–169.

Holt, D., 1970. Dislocation cell formation in metals. J. Appl. Phys. 41, 3197–3201.

Houslby, G.T., Puzrin, A.M., 2000. A thermomechanical framework for constitutive models for rate-independent dissipative materials. Int. J. Plasticity 16, 1017–1048.

Hughes, D.A., Khan, S.M.A., Godfrey, A., Zbib, H.M., 2001. Internal structures of deformation induced planar dislocation boundaries. Mater. Sci. Eng. A309–310, 220–226.

Kalidindi, S.R., 2001. Modeling anisotropic strain hardening and deformation textures in low stacking fault energy fcc metals. Int. J. Plasticity 17, 837–860.

Kamat, S.V., Hirth, J.P., 1990. Dislocation injection in strained multilayer structures. J. Appl. Phys. 67 (11), 6844.

Khan, A., Liang, R., 2000. Behavior of three bcc metals during non-proportional multi-axial loadings: experiments and modeling. Int. J. Plasticity 16, 1443–1458.

Khan, A.S., Chang, P., 1996. Study of three elastic-plastic constitutive models by non-proportional finite deformation of OFHC copper. Int. J. Plasticity 12, 737–760.

Kharishi, T., Zbib, H.M., Diaz de la Rubia, T., 2001. The treatment of traction-free boundary condition in three-dimensional dislocation dynamics using generalized image stress analysis. Mater. Sci. Eng. A309–310, 283–287.

Khraishi, T.A., Zbib, H.M., Hirth, J.P., Khaleel, M., 2000. Analytical solution for the stress-displacement field of glide dislocation loop. Int. J. Eng. Sci. 38, 251–266.

Kratochvil, J., Saxlova, M., Devincre, B., Kubin, L., 1997. On the sweeping of diploar loops by gliding dislocations. Mater. Sci. Eng. A234–236, 318–321.

Kubin, L.P., 1993. Dislocation patterning during multiple slip of fcc crystals. Phys. Stat. Sol (a) 135, 433–443.

Kubin, L.P., Estrin, Y. and Canova, G., 1990. Dislocation patterns and plastic instabilities. In: Walgraef, D., Ghoniem, N. M. (Eds.), Patterns, Defects and Material Instabilities. Kluwer Academic, pp. 277–301.

Kuhlmann-Wilsdorf, D., 1998. Questions you always wanted (or should have wanted) to ask about work hardening. Mat. Res. Innovat. 1, 265.

Lambros, J., Rosakis, A.J., 1995. Development of a dynamic decohesion criterion for subsonic fracture of the interface between two dissimilar materials. SM Report 95–3, Cal. Tech.

Le, K.C., Stumpf, H., 1996. A model of elasticplastic bodies with continuously distributed dislocations. Int. J. Plasticity 12, 611–628.

Lepinoux, J., Kubin, L.P., 1987. The dynamic organization of dislocation structures: a simulation. Scripta Metall. 21, 833–838.

McDowell, D.L., 1992. A nonlinear kinematic hardening theory of cyclic thermoplasticity and thermoviscoplasticity. Int. J. Plasticity 8, 695–728.

Needleman, A., 2000. Computational mechanics at the mesoscale. Acta Mater. 48, 105–124.

Rhee, M., Hirth, J.P., Zbib, H.M., 1994. On the bowed out tilt wall model of flow stress and size effects in metal matrix composites. Acta Metall. Mater. 31, 1321–1324.

Rhee, M., Zbib, H.M., Hirth, J.P., Huang, H., Rubia, T.D.d.L., 1998. Models for long/short range interactions in 3D dislocatoin simulation. Modeling & Simulations in Mater. Sci. & Eng. 6, 467–492.

Scattergood, R.O., Bacon, D.J., 1975. The Orwan mechanism in ansiotropic crystal. Phil. Mag. 31, 179–198.

Scheidler, M., Wright, T.W., 2001. A continuum framework for finite viscoplasticity. Int. J. Plasticity 17, 1033–1085.

Shizawa, K., Zbib, H.M., 1999. Thermodynamical theory of strain gradient elastoplasticity. Dislocation Density: Part I—Fundamentals. Int. J. Plasticity 15, 899–938.

Urabe, N., Weertman, J., 1975. Dislocation mobility in potassium and iron single crystals. Mater. Sci. Eng. 18, 41.

Van der Giessen, E., Needleman, A., 1995. Discrete dislocation plasticity: a simple planar model. Modelling simul. Mater. Sci. Eng. 3, 689–735.

Voyadjis, G.Z., Mohammad, L.M., 1991. Theory vs experiment for finite strain viscoplastic Lagrangian constitutive model. Int. J. Plasticity 7, 329–350.

Walgraef, D., Schiller, C., 1987. Anisotropy effects on pattern selection near dynamical instabilities. Phisica D 27, 423–432.

Wang, H.Y., LeSar, R., 1995. O(N) algorithm for dislocation dynamics. Phil. Mag. A 71, 149–164.

Yasin, H., Zbib, H.M., Khaleel, M.A., 2001. Size and boundary effects in discrete dislocation dynamics: coupling with continuum finite element. Mater. Sci. Eng. A309–310, 294–299.

Zbib, H.M., Jubran, J.S., 1992. Dynamic shear banding: a three-dimensional analysis. Int. J. Plasticity 8, 619–641.

Zbib, H.M., Rhee, M., Hirth, J.P., 1996. 3D simulation of curved dislocations: discretization and long range interactions. In: Abe, T., Tsuta, T. (Eds.), Advances in Engineering Plasticity and its Applications. Pergamon, New York, pp. 15–20.

Zbib, H.M., Rhee, M., Hirth, J.P., 1998. On plastic deformation and the dynamcis of 3D dislocations. Int. J. Mech. Science 40, 113–127.

Zielinski, W., Huang, H., Venkatarman, S., Gerberich, W.W., 1995. Dislocation distribution under a microindentation into an iron-silicon single crystal. Phil. Mag. A 72, 1221–1237.